A second-order-accurate immersed boundary ghost-cell method with hybrid reconstruction for compressible flow simulations

Xinxin Wang[a], Ralf Deiterding[b], Jianhan Liang[a,*], Xiaodong Cai[a,**], Wandong Zhao[a]

[a] *Science and Technology on Scramjet Laboratory, National University of Defense Technology, Hunan, China*
[b] *Aerodynamics and Flight Mechanics Research Group, University of Southampton, Boldrewood Innovation Campus, Southampton SO16 7QF, United Kingdom*

Abstract

This study presents an improved ghost-cell immersed boundary method for geometrically complex boundaries in compressible flow simulations. A bilinearly complete extrapolation scheme is developed for the reconstruction of the ghost cell. The second-order accuracy of the improved ghost-cell method (GCM) is shown in unit test cases and is also theoretically proven. A hybrid GCM based on both baseline GCM and improved GCM is proposed and constructed. The hybrid GCM applied in compressible flow is validated against five test cases: (a) Stationary rotating vortex, (b) Prandtl-Meyer expansion flow, (c) Double Mach reflection, (d) Moving-shock/obstacle interaction, (e) Blunt body shock-induced combustion. This paper provides a comprehensive comparison of their performance in terms of various accuracy and computation time measurements. The simulation results demonstrate that the hybrid GCM has higher accuracy and convergence than the remaining two GCMs in all cases. By directly comparing the primitive variables along the boundary, it can be concluded that the hybrid GCM has significant advantages in compressible flow simulations. The results of CPU time show that the hybrid GCM can provide more accurate results while ensuring the efficiency of the calculation.

Keywords: Cartesian grid, ghost-cell method, level-set method, immersed boundary

*Corresponding author
**Corresponding author
Email addresses: jhleon@vip.sina.com (Jianhan Liang), cai-chonger@hotmail.com (Xiaodong Cai)

1. Introduction

There has been extensive research on computational fluid dynamics (CFD) simulations employing complex geometries within the computational domain in recent years. Traditionally, the solid boundary is approximated with body-fitted grids, structured or unstructured. The main disadvantage of body-fitted grids is that much effort must be put into the pre-processing stage. In recent years, researchers have shown an increased interest in using Cartesian grids for simulations. One of the main obstacles is that the complex geometries do not coincide with the Cartesian grid. Immersed boundary (IB) methods are among the most widely used Cartesian grid methods for dealing with complex boundaries. The importance of immersed boundary methods is indisputable.

The immersed boundary method (IBM) proposed by Peskin [1, 2, 3] is employed to handle elastic boundaries for simulating blood flow in the heart. A recent systematic literature review [4] refers to this method as the "continuous forcing method". The forcing is incorporated into the continuous equations before discretization. This method is suitable for the case where the boundary is elastic, and the Dirac delta function used for the elastic boundary does not fit well with the rigid boundary in general [4].

The discrete forcing approach is proposed to overcome the problem that the elastic force source term cannot be given precisely in the Navier-Stokes (NS) governing equations [4]. The discrete forcing approach is implemented by modifying the computational stencil localized at the difference scheme boundary and imposing the boundary conditions on the immersed boundary. The discrete forcing approach can reconstruct the boundary accurately. Previous research has established two approaches to modify the computational stencil: cut-cell methods (CCM) and ghost-cell methods (GCM).

Cut-cell methods based on finite volume IB methods–in comparison to finite difference ghost cell methods–are attractive as they enforce strict conservation of mass, momentum and energy [5, 6, 7]. The primary issue however is the

presence of small cells, which results in an excessively small time step in case of an explicit scheme or a poorly conditioned matrix in case of an implicit scheme [7].

The concept of GCM is most commonly associated with the works of Mohd-Yusof [8] and Fadlun [9]. The boundary condition on the IB is enforced through the ghost-cells. Ghost-cells are defined as cells in the solid that have at least one neighbor in the fluid. For each ghost-cell, an interpolation scheme that implicitly incorporates the boundary condition on the IB is then devised [4]. Different interpolation procedures for the mirror point [10] and extrapolation procedures for the ghost point [11] can be utilized to obtain a second or even higher order accuracy [12, 13, 14, 15]. A simple GCM interpolation scheme [16] is bilinear interpolation using the information of surrounding fluid nodes. However, at high Reynolds numbers, when the resolution is marginal, linear reconstruction could lead to erroneous predictions [4]. An improved method [17] employs a linear interpolation in the tangential and a quadratic interpolation in the normal direction. Felten et al. [18] demonstrated that interpolation errors do not significantly affect the results as long as the simulation has a sufficiently fine grid and short time steps. A seminal study in this area was the work of Tseng et al. [10] who proposed methods to solve the incompressible NS equation by an implicit pressure-corrected finite volume method on Cartesian grids. Tseng et al. [10] studied the effects of the local stencil near the boundary for the problem when too few points are available for interpolation. Pan et al. [19, 20, 21] proposed a simple and stable ghost-cell method which was developed to treat the boundary condition for the immersed bodies in the flow field. Pan et al. demonstrated that the spatial accuracy of the method is second-order-accurate in the L_2 norm for both velocity and pressure. The GCM has shown large potential to handle different fluid-solid interaction problems, including those with moving objects [22, 23, 24] and highly complex geometries [25, 26, 27, 15]. Ji et al. [28] tested the hypersonic blunt-body shock-induced combustion phenomenon employing the cut-cell method with second-order accuracy and proved the accuracy by merging the cut cells to cope with the small-cell problem. Combining the

immersed boundary method with adaptive mesh refinement (AMR) improves accuracy of numerical simulations considerably. Deiterding et al. [29] used the ghost-cell method with AMR techniques to improve computational efficiency in the case of hypersonic blunt-body flows. These studies [30, 31, 32] showed good results regarding the robustness and accuracy of the ghost-cell method.

However, the simple GCM method [18] suffers from an issue by reconstructing the value at ghost-cells that are too close to the boundary. Chi et al. [33, 34] proposed an improved method whose ghost-cells are mirrored through the boundary to farther image points. In this paper, a general boundary condition treatment based on the idea of Chi et al.[33, 34] is developed and validated. The concept of the image point is adopted and modified to construct a simple and stable bilinear reconstruction scheme. A new reconstruction stencil is carried out to eliminate some of the assumptions of the method as given in previous publications [33, 34]. The main advantage of the current approach is the ease of programming, which requires only that an improved reconstruction stencil be added to an existing code.

This paper is organized as follows: Section 2 introduces the computational model, including governing equations, numerical methods, improved ghost-cell method and hybrid method. Section 3 compares and verifies the applicability of the hybrid method for a number of cases: unit test, stationary rotating vortex, Prandtl-Meyer expansion wave, double Mach reflection, moving-shock/obstacle interaction and blunt body shock-induced combustion. All GCM methods in this section are implemented in the AMROC framework [35, 36, 37]. The CCM method used for comparison is implemented in the AMReX framework [38]. Section 4 concludes the paper.

2. Computational Model

2.1. Governing equations and numerical method

The two-dimensional Euler equations governing fully compressible flows read as follows [39]:

$$\frac{\partial U}{\partial t}+\frac{\partial F(U)}{\partial x}+\frac{\partial G(U)}{\partial y}=0 \tag{1}$$

$$U=(\rho,\rho u,\rho v,E)^{T} \tag{2}$$

$$F(U)=\begin{pmatrix}\rho u\\ \rho u^{2}+p\\ \rho uv\\ u\left(E+p\right)\end{pmatrix}\quad G(U)=\begin{pmatrix}\rho v\\ \rho uv\\ \rho v^{2}+p\\ v\left(E+p\right)\end{pmatrix}$$

With the ideal gas equation of states, total specific energy E and speed of sound a are written as

$$E=\frac{p}{\gamma-1}+\frac{1}{2}\rho u^{2},\quad a=\sqrt{\frac{\gamma p}{\rho}} \tag{3}$$

Van Leer [40] achieved higher accuracy by modifying the constant data of a scheme based on the first-order Godunov method, which has been called MUSCL (Monotone Upstream Centred Scheme for Conservation Laws). MUSCL is a classical high-order approach that can be constructed with higher accuracy than second-order and is widely used in numerical simulations. The MUSCL-Hancock scheme[40, 39] is used to approximate the primitive variables as follows:

Step (I) Reconstruct the left and right values:

$$u_{i}^{L}=u_{i}^{n}-\frac{1}{2}\Delta_{i},\quad u_{i}^{R}=u_{i}^{n}+\frac{1}{2}\Delta_{i} \tag{4}$$

Step (II) Calculate the value at the time of $\frac{1}{2}\Delta t$:

$$\left.\begin{aligned}\bar{u}_{i}^{L}&=u_{i}^{L}+\tfrac{1}{2}\tfrac{\Delta t}{\Delta x}\left[f\left(u_{i}^{L}\right)-f\left(u_{i}^{R}\right)\right]\\ \bar{u}_{i}^{R}&=u_{i}^{R}+\tfrac{1}{2}\tfrac{\Delta t}{\Delta x}\left[f\left(u_{i}^{L}\right)-f\left(u_{i}^{R}\right)\right]\end{aligned}\right\} \tag{5}$$

Step (III) Solve the Riemann problem with segmented constants:

$$\left.\begin{array}{l} u_t + f(u)_x = 0 \\ u(x,0) = \left\{ \begin{array}{ll} \bar{u}_i^R, & x < 0 \\ \bar{u}_{i+1}^L, & x > 0 \end{array} \right. \end{array}\right\} \tag{6}$$

As for the linear advection equation $f(u) = au$, the fluxes constructed by the MUSCL-Hancock method are represented as:

$$f_{i+\frac{1}{2}}^{MHM} = \frac{1}{2}(1+\text{sign}(c))f\left(\bar{u}_i^R\right) + \frac{1}{2}(1-\text{sign}(c))f\left(\bar{u}_{i+1}^L\right) \tag{7}$$

$$f\left(\bar{u}_i^R\right) = a\left[u_i^n + \frac{1}{2}(1-c)\Delta_i\right], \quad f\left(\bar{u}_{i+1}^L\right) = a\left[u_{i+1}^n - \frac{1}{2}(1+c)\Delta_{i+1}\right] \tag{8}$$

where c is the Courant number.

In order to avoid the correction of the Riemann solver for the immersed method, this study adopts the primitive variable Riemann solver (PVRS) [39]. The format of this approximate Riemann solver is as follows:

$$p_* = \frac{C_R p_L + C_L p_R + C_L C_R (u_L - u_R)}{C_L + C_R}, \quad u_* = \frac{C_L u_L + C_R u_R + (p_L - p_R)}{C_L + C_R} \tag{9}$$

$$\rho_{*L} = \frac{\rho_L + (p_* - p_L)}{a_L^2}, \quad \rho_{*R} = \frac{\rho_R + (p_* - p_R)}{a_R^2} \tag{10}$$

where

$$a_{L,R}^2 = \gamma \frac{p_{L,R}}{\rho_{L,R}}, \quad C_{L,R} = \sqrt{\gamma p_{L,R} \rho_{L,R}} \tag{11}$$

In the above, L, R represents the left and right states for the Riemann problem.

2.2. The level-set method

The necessary geometric information needs to be stored for the ghost-cell projection process to accurately represent the solid wall boundary intersecting with the Cartesian grid. There are many methods for interface tracking, and general methods include the marker-and-cell method proposed by McKee et al. [41], the front-tracking method proposed by Tryggvason et al. [42], the

volume-of-fluid method proposed by Lörstad et al. [43], and the level-set method proposed by Osher and Fedkiw et al. [44, 45]. The level-set methods [44, 3, 46, 45, 47] handle interfacial evolutions automatically and interface curvature and normal are easily dealt with. The level-set method is thus chosen as the interface capturing scheme in this study. The AMROC framework represents geometry implicitly through a level-set function. There are many different level-set methods and they usually have in common that the level set is updated with a finite difference advection scheme to represent the interfacial evolution, for instance, a multi-phase flow.

The level-set method is the primary interface tracking method, which defines the solid-fluid marker variables as a distance function from the boundary. In this method, the interface is represented by a zero-valued equivalence surface of the distance function, continuously distributed over the interface. Compared with the volume of fluid method, the normal and curvature of the boundary can be calculated more accurately. In terms of the level-set method, the direction of the boundary at each time step is determined directly from the level-set variable distribution.

The distance function is defined as: $d(\mathbf{x}) = \min(|\mathbf{x} - \mathbf{x}_I|)$, where $\mathbf{x}_I$ represents the intersection of the fluid and the solid. The interface is a zero-level set of ϕ:

$$\Gamma = \{\mathbf{x} \mid \phi(\mathbf{x}, t) = 0\} \tag{12}$$

where $\phi > 0$ is taken in the fluid region and $\phi < 0$ in the solid region:

$$\phi(\mathbf{x}, t) \begin{cases} > 0 & \text{if } \mathbf{x} \in \text{ Fluid} \\ = 0 & \text{if } \quad \mathbf{x} \in \Gamma \\ < 0 & \text{if } \mathbf{x} \in \text{ Solid} \end{cases} \tag{13}$$

Two dimensional, stationary level-set cases are considered in the present study. Therefore the position of the interface is independent of time, i.e. $\phi(\mathbf{x}, t) = \phi(\mathbf{x})$. The boundary normal and interface curvature can be easily expressed in terms of $\phi(\mathbf{x}, t)$:

$$\mathbf{n} = \left.\frac{\nabla\phi}{|\nabla\phi|}\right|_{\phi=0}, \quad \kappa = \nabla \cdot \left.\left(\frac{\nabla\phi}{|\nabla\phi|}\right)\right|_{\phi=0} \tag{14}$$

In Cartesian coordinates, the derivative $\nabla\phi$ in Eq. (14) needs to be approximated. For computational accuracy in the current calculation, we use the second-order central difference format:

$$\frac{\partial \phi}{\partial x} \approx \frac{\phi_{x+\Delta x} - \phi_{x-\Delta x}}{2\Delta x} \tag{15}$$

The degree of accuracy of the unit normal depends on the grid size in the calculation. The central differencing has second-order accuracy and can usually be combined with AMR.

2.3. Improved ghost-cell method

2.3.1. Ghost-cell reconstruction

The classic bilinear interpolation scheme available in the AMROC package [36] is referred to as the base ghost-cell method [33]. In the base ghost-cell method, the mirror points of the ghost point are mirrored symmetrically by the boundary such that:

$$r_M = r_G \tag{16}$$

A ghost point is defined as the center point of a ghost-cell. The image point is the symmetry point of the ghost point in the fluid region near the boundary. The projection point is the normal projection of the ghost point at the boundary. r_M is the absolute distance from the projection point to the image point, and r_G is the absolute distance from the projection point to the ghost point.

The state values at the image point can then defined using a bilinear interpolation from surrounding cell-centered values available in the fluid. When the location of the image point of the ghost point and the physical quantities are determined, the slip wall boundary conditions of the projection point can be applied to construct the ghost point, as follows:

$$\mathbf{q}_{image} = \mathbf{q}_{ghost}, \quad u_n|_{ghost} = -u_n|_{image}, \quad u_t|_{ghost} = u_t|_{image} \tag{17}$$

where u_n is the velocity normal to the wall, $\mathbf{q}$ denotes other physical quantities including the tangential velocity of the wall u_t. The no-slip wall boundary

conditions can be represented as:

$$\mathbf{q}_{image} = \mathbf{q}_{ghost}, \quad u_n|_{ghost} = -u_n|_{image}, \quad u_t|_{ghost} = -u_t|_{image} \tag{18}$$

The base method is easily implemented, with small computational burden thanks to its simple structure and strong robustness [37].

The baseline method provides an incomplete bilinear interpolation when the ghost-cell is too close to the boundary, as shown in Figure 1. The above reason will cause the interpolation accuracy to be significantly reduced. Pan and

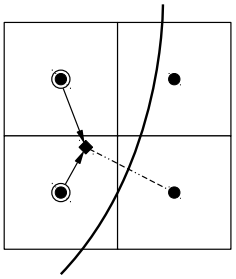

Figure 1: The number of interpolation points becomes fewer when the image points are closer to the boundary

Shen [19] introduced an improved method to ensure complete bilinear interpolations for incompressible flows, and Chi et al. [33] extended its application to compressible flows. However, uncertainties are introduced by simplified model assumptions in the Chi et al. method [33]. Therefore, this study extends this stencil to a more general form in compressible flows to avoid excessive assumptions. An improved ghost-cell value reconstruction method is proposed based on the Cheng et al. stencil. The improved reconstruction method proposed in this study can guarantee complete bilinear interpolation and hence has second-order accuracy.

The image point is projected to a farther fluid domain when the distance is less than a threshold, as shown in Figure 2(a). The distance δ should be far enough to ensure that the image point can be surrounded by the four neighboring fluid cell central points. However, a large unrestricted distance δ may result in severe errors in the extrapolation to the ghost point. Therefore, the threshold

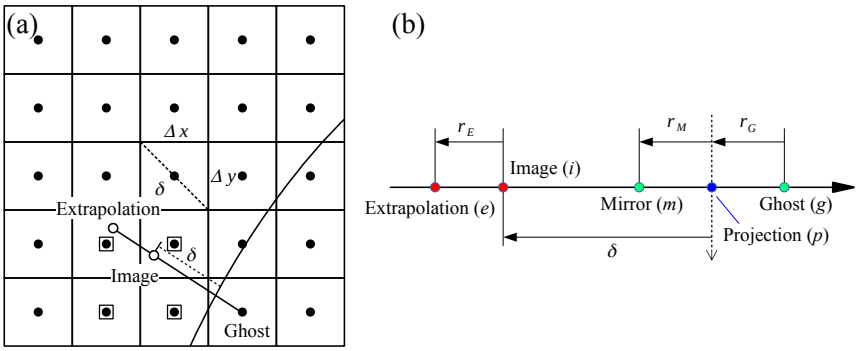

Figure 2: Schematic diagram of the improved ghost-cell method

distance δ is suggested as $\delta = \sqrt{2}\Delta x$ in the two-dimensional case, where Δx is the grid size [33].

The one-dimensional model of the method is shown in Figure 2(b), where vector $\mathbf{q}_g$ represents the primitive variables of ghost point; vector $\mathbf{q}_e$ represents the primitive variables of the extrapolation point; vector $\mathbf{q}_i$ represents the primitive variables of the projected image point; vector $\mathbf{q}_m$ represents the primitive variables of the symmetric mirror point; vector $\mathbf{q}_p$ represents the primitive variables of the projection point; r_E is the absolute distance from the image point to the extrapolation point; r_M is the absolute distance from the symmetric mirror point to the projection point; r_G is the absolute distance from the ghost point to the projection point. The location of the ghost point and the mirror point are symmetrical about the boundary, which can be directly derived as $r_M = r_G$. For simplicity, the location of the extrapolation image point is defined as $r_E = r_G$.

The primitive variables of the image and extrapolation points can be bilinearly interpolated from the surrounding nodes. A Neumann boundary condition is adopted to deal with the solid boundaries and the normal gradient of the projection point is zero.

The primitive variables of image points, extrapolation points, and projection points adopt the second-order Taylor expansion as follows:

$$\mathbf{q_i} = \mathbf{q_m} + (\delta - r_G) \cdot \left.\frac{\partial \mathbf{q}}{\partial \mathbf{n}}\right|_m + \frac{(\delta - r_G)^2}{2} \cdot \left.\frac{\partial^2 \mathbf{q}}{\partial \mathbf{n}^2}\right|_m + R_{n1} \tag{19}$$

$$\mathbf{q_p} = \mathbf{q_m} - r_G \cdot \left.\frac{\partial \mathbf{q}}{\partial \mathbf{n}}\right|_m + \frac{r_G^2}{2} \cdot \left.\frac{\partial^2 \mathbf{q}}{\partial \mathbf{n}^2}\right|_m + R_{n2} \tag{20}$$

$$\mathbf{q_e} = \mathbf{q_m} + (\delta + r_E - r_G) \cdot \left.\frac{\partial \mathbf{q}}{\partial \mathbf{n}}\right|_m + \frac{(\delta + r_E - r_G)^2}{2} \cdot \left.\frac{\partial^2 \mathbf{q}}{\partial \mathbf{n}^2}\right|_m + R_{n3} \tag{21}$$

where $R_{n1} = o\left((\delta - r_G)^2\right)$, $R_{n2} = o\left(r_G^2\right)$, $R_{n3} = o\left((\delta + r_E - r_G)^2\right)$

Equation system (19-21) can be further written as the following matrix form:

$$\begin{pmatrix} 1 & \delta - r_G & \frac{(\delta - r_G)^2}{2} \\ 1 & -r_G & \frac{r_G^2}{2} \\ 1 & \delta + r_E - r_G & \frac{(\delta + r_E - r_G)^2}{2} \end{pmatrix} \begin{pmatrix} \mathbf{q_m} \\ \left.\frac{\partial \mathbf{q}}{\partial \mathbf{n}}\right|_m \\ \left.\frac{\partial^2 \mathbf{q}}{\partial \mathbf{n}^2}\right|_m \end{pmatrix} = \begin{pmatrix} \mathbf{q_i} - R_{n1} \\ \mathbf{q_p} - R_{n2} \\ \mathbf{q_e} - R_{n3} \end{pmatrix} \tag{22}$$

It can be deduced that for $\mathbf{q_m}$ the formula reads as follows:

$$\mathbf{q_m} = \frac{\mathbf{q_e}\delta r_G (r_G - \delta) + \mathbf{q_i} r_G (r_E + \delta - r_G)(r_E + \delta) + \mathbf{q_p} r_E (r_G - \delta)(r_E - r_G + \delta)}{\delta(r_E^2 + \delta r_E)} + R_{t1} \tag{23}$$

The error R_{t1} can be written as

$$R_{t1} = \frac{R_{n1} r_G (\delta + r_E - r_G)(\delta + r_E) + R_{n2} r_E (\delta - r_G - r_E)(\delta - r_G) + R_{n3}\delta r_G (r_G - \delta)}{\delta(r_E^2 + \delta r_E)} \tag{24}$$

The value of $\mathbf{q_p}$ is unknown. The second-order Taylor expansion can be adopted at $\mathbf{q_i}$ and $\mathbf{q_e}$ to solve $\mathbf{q_p}$:

$$\mathbf{q_i} = \mathbf{q_p} + \delta \cdot \left.\frac{\partial \mathbf{q}}{\partial \mathbf{n}}\right|_p + \frac{\delta^2}{2} \cdot \left.\frac{\partial^2 \mathbf{q}}{\partial \mathbf{n}^2}\right|_p + R_{n4} \tag{25}$$

$$\mathbf{q_e} = \mathbf{q_p} + (\delta + r_E) \cdot \left.\frac{\partial \mathbf{q}}{\partial \mathbf{n}}\right|_p + \frac{(\delta + r_E)^2}{2} \cdot \left.\frac{\partial^2 \mathbf{q}}{\partial \mathbf{n}^2}\right|_p + R_{n5} \tag{26}$$

where $R_{n4} = o\left(\delta^2\right)$, $R_{n5} = o\left((\delta + r_E)^2\right)$.

Imposing boundary conditions, $\frac{\partial \mathbf{q}}{\partial \mathbf{n}} = 0$, Eq. (26) can be written as:

$$\begin{pmatrix} 1 & \frac{\delta^2}{2} \\ 1 & \frac{(\delta + r_E)^2}{2} \end{pmatrix} \begin{pmatrix} \mathbf{q_p} \\ \left.\frac{\partial^2 \mathbf{q}}{\partial \mathbf{n}^2}\right|_p \end{pmatrix} = \begin{pmatrix} \mathbf{q_i} - R_{n4} \\ \mathbf{q_e} - R_{n5} \end{pmatrix} \tag{27}$$

$\mathbf{q_p}$ can be solved for:

$$\mathbf{q_p} = \frac{\mathbf{q_i}\left(\delta + r_E\right)^2 - \mathbf{q_e}\delta^2}{r_E^2 + 2\delta r_E} + R_{t2} \tag{28}$$

The error R_{t2} can be written as

$$R_{t2} = \frac{R_{n4}\left(\delta + r_E\right)^2 - R_{n5}\delta^2}{r_E^2 + 2\delta r_E} \tag{29}$$

Replacing Eq. (28) into Eq. (25) yields:

$$\mathbf{q_m} = \frac{\mathbf{q_i}\left(\left(\delta + r_E\right)^2 - r_G^2\right) - \mathbf{q_e}\left(\delta^2 - r_G^2\right)}{r_E^2 + 2\delta r_E} + R_{t3} \tag{30}$$

The error R_{t3} can be written as

$$\begin{aligned} R_{t3} =& \frac{r_G\left(\delta + r_E - r_G\right)}{\delta r_E} R_{n1} + \frac{\left(\delta - r_G\right)\left(\delta + r_E - r_G\right)}{\delta\left(\delta + r_E\right)} R_{n2} - \frac{\left(\delta - r_G\right) r_G}{r_E\left(\delta + r_E\right)} R_{n3} \\ &+ \frac{\left(\delta + r_E\right)\left(\delta - r_G\right)\left(\delta + r_E - r_G\right)}{\delta r_E\left(2\delta + r_E\right)} R_{n4} - \frac{\delta\left(\delta - r_G\right)\left(\delta + r_E - r_G\right)}{r_E\left(2\delta + r_E\right)\left(\delta + r_E\right)} R_{n5} \end{aligned} \tag{31}$$

Substituing $\mathbf{q_p} = 0$ into Eq. (23), the normal component of the velocity u_n is derived as follows:

$$u_{mn} = \frac{u_{en}\delta r_G\left(r_G - \delta\right) + u_{in} r_G\left(r_E + \delta - r_G\right)\left(r_E + \delta\right)}{\delta(r_E^2 + \delta r_E)} \tag{32}$$

where u_{mn}, u_{en}, u_{in} are the normal components of the velocity of points mirror, extrapolation and image.

Therefore, the second-order-accurate extrapolation formula can be obtained by applying Taylor expansion. The method described above requires no assumption regarding flow properties and is therefore more generally applicable. Using Eqs. (23), (32), the values of the mirror points can be derived when the values of the image points and the extrapolation points are known. The primitive variables of the image points and the extrapolation points can be interpolated from the surrounding flow field cell centers by using a complete bilinear interpolation.

2.3.2. Hybrid improved GCM

While the improved method deals with the interpolation challenge listed above, there is still room for improvement. It can be seen from Eq. (31) that

the analytical error is $R \propto o\left((\delta + r_E)^2\right)$. The accuracy of the improved GCM is dependent on the distance between the extrapolation points and the boundary. The accuracy of the improved GCM is dependent on the distance between the extrapolation points and the boundary. If the mirror point can be completely bilinearly interpolated from surrounding cells, the improved GCM would not be necessary. This leads to the issue of whether the improved method is applicable to all mirror points.

A simple improvement to the issue involves developing a hybrid method that combines the results from different methods. The proposed approach can be interpreted as a hybrid baseline/improved method, in which the conventional baseline method is used to deal with suitable distance cells, whereas the improved method is used to handle cells too close to the boundary.

If the global improved method is adopted, it is called the general bilinear complete ghost-cell method (BCGCM) in the following. The hybrid method is called the hybrid bilinear complete ghost-cell method (HBCGCM).

To evaluate the accuracy of the boundary treatment methods, a norm of a solution residual ε is defined as follows:

$$\|\varepsilon\|_p = \left[\frac{\sum_i^N |\varepsilon_i|^p}{N}\right]^{\frac{1}{p}} \tag{33}$$

where $\sum_i^N$ denotes the summation over all cells in the computational domain. The L_1 , L_2 and L_∞ norm of ε are defined respectively when $p = 1, 2$, or ∞. The order of convergence of the solution is derived by considering the difference between solution residuals obtained on different Cartesian grid sizes as

$$r_p = \frac{log(\frac{\|\varepsilon_1\|_p}{\|\varepsilon_2\|_p})}{log(\frac{h_1}{h_2})} \tag{34}$$

where ε_1 and ε_2 are the solution residuals obtained on two grids with spacings h_1 and h_2, respectively.

3. Verification

In this section, the results of verification cases are presented with the method proposed in Section 2. The results of the unit test are first presented to analyze the accuracy of the improved method. Next, stationary rotating vortex and Prandtl-Meyer expansion wave cases are employed to verify the accuracy of the HBCGCM in compressible flows. The double Mach reflection case verifies the capability of the HBCGCM in discontinuities. Finally, the capability of the HBCGCM in Euler equations with reaction is demonstrated by the blunt body shock-induced combustion case.

3.1. Unit tests

The unit test is a visual case to illustrate the analytical accuracy performance. In this case, the ghost-cell is not in actual compressible flows. This case is used to compare the accuracy of reconstruction directly. In the unit test, the accuracy of the baseline method, the improved method and Chi method are compared. ~~The accuracy of the HBCGCM is compared with that of the other methods in complex geometric boundaries problems.~~ In this case, the improved method was processed with only a single ghost-cell in order to test its performance and compare it under the same conditions as the other approaches. In the current setup, a random boundary is considered as shown by the dashed lines in Figure 3. The level-set function of the boundary is derived as follows

$$\phi(\mathbf{x}_{ghost}) = -\phi(\mathbf{x}_{mirror}) \tag{35}$$

Once the position of the random mirror point $\mathbf{x}_{mirror} = (x_m, y_m)$ is determined, the position of the boundary and the rest of the points can be fixed. When setting the mirror point, it is necessary to ensure that the surrounding nodes are not all in the fluid to represent the incomplete bilinear interpolation. A predefined function is employed in the computational domain rather than the governing equations.

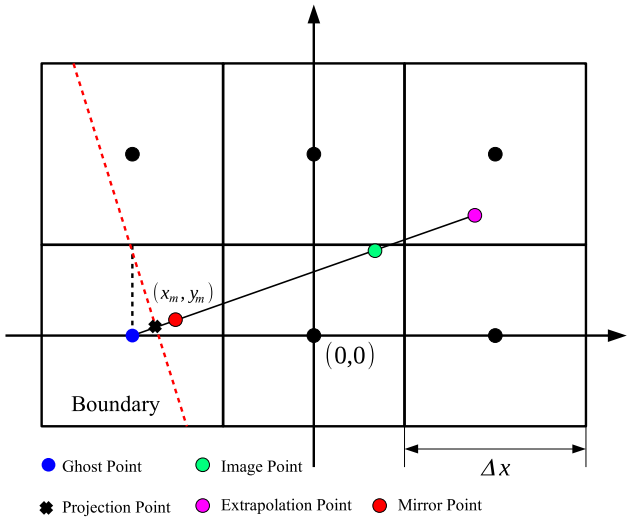

Figure 3: Unit test model

Three predefined functions are employed: primary function, fourth-order polynomial function and cosine function, as follows:

$$\begin{aligned} &(1) \quad a_1 x + a_2 y + a_3 + kx + y \\ &(2) \quad a_1 x^4 + a_2 y^4 + a_3 x^2 y^2 + a_4 x^3 y + a_5 x y^3 + \ldots + a_{15} + kx + y \\ &(3) \quad a_1 \cos(x+y) + a_2 \cos(x) + a_3 \sin(y) + kx + y \end{aligned} \tag{36}$$

The coefficient a_i is taken as a random number between 0 and 1 in the test. To guarantee the Neumann boundary conditions, the gradient of primitive variables normal to the boundary needs to be 0. The gradient of the primitive variables at the boundary is expressed in the form of a_i and k. a_i is a random number and is known. Thus, k can be solved to ensure that the gradient is 0.

First, the improved method was tested in terms of pure extrapolation accuracy. The pure extrapolation means that the image point and the extrapolation point are both exact values. The source of error is only related to the extrapolation of the two points to the mirror point in the pure extrapolation method. The exact values of each point are determined by evaluating the predefined function. The absolute values of the errors of the improved method, Chi method and lin-

ear method are compared, where the linear method refers to the direct linear extrapolation of the image points and extrapolation points to the values of the mirror points.

The coordinates of the mirror point vary between $x \in [-\Delta x, \frac{-\Delta x}{2}]$, $y \in [0, \frac{\Delta y}{2}]$. The grid size is gradually reduced from 1 to 10^{-5} to compare the errors of extrapolation at the mirror point for different grid sizes. Each test function is repeated 1000 times. 1000 randomly generated coefficient datasets are adopted for each predefined function to correspond to a random location. The errors of the three methods are shown in Figure 4.

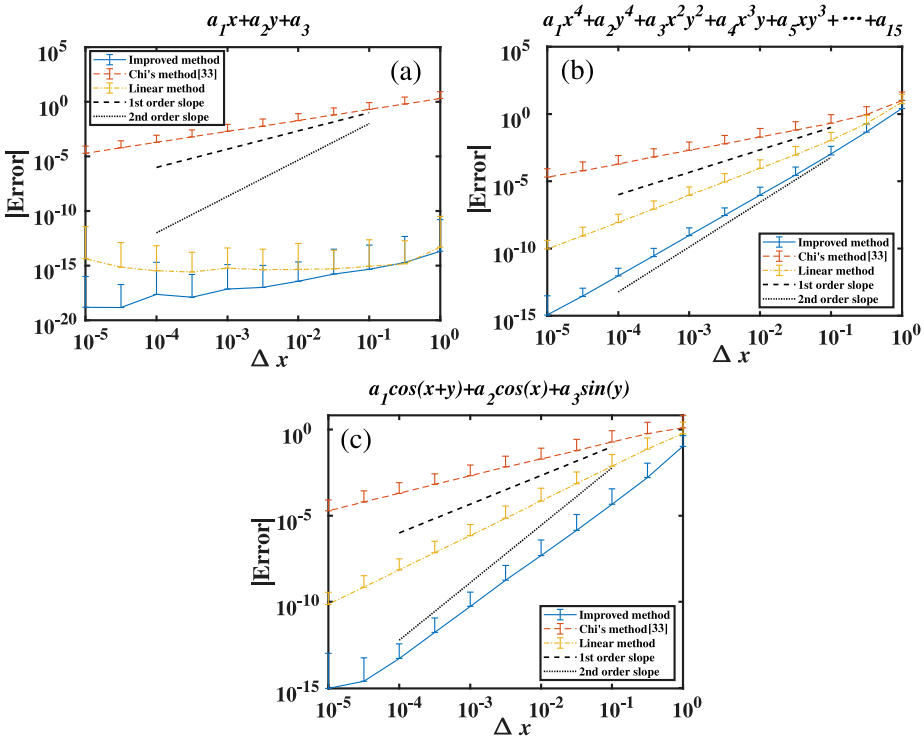

Figure 4: Variation of the absolute value of the error with the grid size in pure extrapolation tests for different test functions, (a) test function 1 (b) test function 2 (c) test function 3

As shown in Figure 4, each value represents the mean of 1000 independent experiments, and the error bars represent the standard deviations. Figure 4

shows that the improved method significantly outperforms the Chi method and the linear method for the three types of test functions. The improved method is at least one order of magnitude better than the others method. As shown in Figure 4(a), the error may not be less than 10^{-20} due to rounding error. The improved method can be considered virtually error-free when dealing with the extrapolation of a linear function. The order of error can be calculated. In test function 2, the mean orders of the improved method and linear method are 2.97 and 1.92, respectively. In test function 3, the mean orders are 3.02 and 1.96. This proves quantitatively that the improved method is second-order-accurate in pure extrapolation. Although the Chi method is a second-order theoretical method, the test function does not satisfy the assumptions required by the Chi method. It results in the unavailability of the second-order Chi method. Thus, the Chi method performs even worse than the linear method in all tests.

Next, the accuracy of complete interpolation is tested. The values of the image and extrapolation points are bilinearly interpolated using the surrounding fluid nodes. When specific assumptions are not satisfied, the accuracy of the Chi method will drop. Consequently, only the accuracy of the baseline method and the improved GCM method are compared in the subsequent tests. The selection of mirror points is similar to the above test. Each test function is still repeated 1000 times.

As shown in Figure 5, the improved method has higher accuracy than the baseline method for all test functions. In test function 2, the mean orders of the improved method and linear method are 2.02 and 1.09, respectively. In test function 3, the mean orders are 2.11 and 0.96. The orders prove that the improved method still has second-order accuracy in this test. The baseline method arrives at low accuracy in the case of incomplete bilinear interpolation. It is worth noting that in Figure 5(b), the baseline method outperforms the improved method for a grid size that is close to 10^0. At the grid size of 1, the distance from the image point to the boundary is greater than $\sqrt{2}$ according to $r_G = \delta = \sqrt{2}\Delta x$. The x and y coordinates of the image point and the extrapolation point may be greater than 1, respectively. The given test function

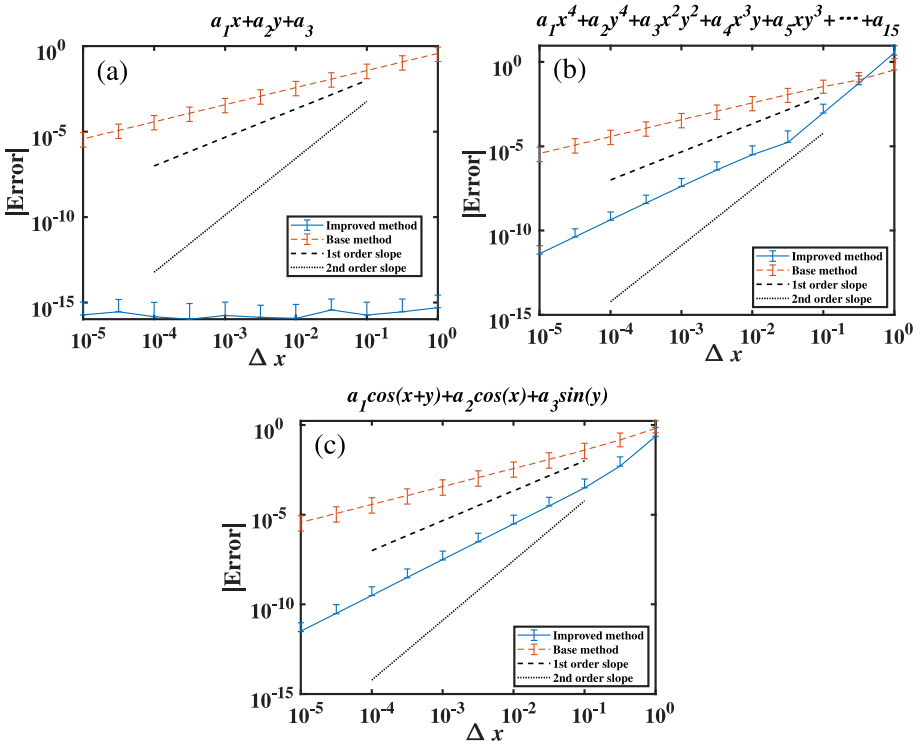

Figure 5: Variation of the absolute value of the error with the grid size in complete interpolation tests for different test functions, (a) test function 1 (b) test function 2 (c) test function 3

is a higher-order polynomial function, which will lead to a sharp change in the function value. The extrapolation is sensitive because it only has two data for the extrapolation. At the same time, the x and y coordinates of the mirror point are less than 1, and the bilinear interpolation function is in a more moderate range. The bilinear interpolation error is significant because the function values around the image point and the extrapolation point change drastically, resulting in a loss of accuracy. The results around 10^0 are related to the selection of grid coordinates, but not to the boundary treatment method. However, these issues would hardly occur during an actual flow field in the numerical simulation since sufficiently fine grids are generally utilized to guarantee convergence. In the

above, the accuracy of the improved method is significantly improved over the baseline method for each test function.

The coordinates of the mirror point vary between $x \in [-\Delta x, \frac{-\Delta x}{2}]$, $y \in [0, \frac{\Delta y}{2}]$. Correspondingly, the slope of the boundary changes with the mirror point coordinates. $\mathbf{q_i}$ and $\mathbf{q_e}$ use the values interpolated from the surrounding nodes, compared to the $\mathbf{q_m}$ incomplete linear interpolation. The grid size is selected as 0.01.

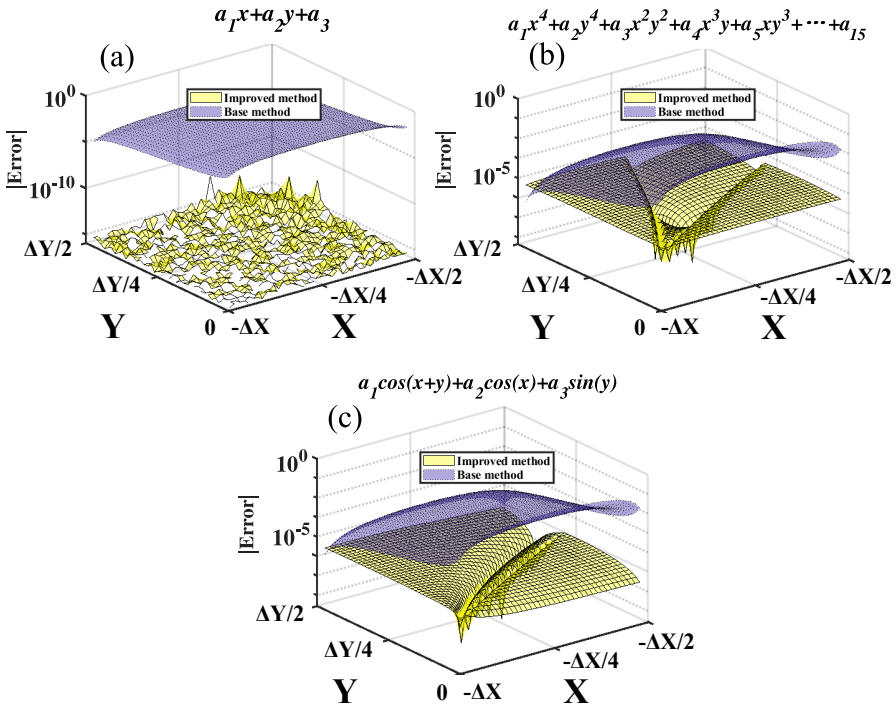

Figure 6: Variation of the absolute value of the error with the mirror point position in complete interpolation tests for different test functions, (a) test function 1 (b) test function 2 (c) test function 3

As shown in Figure 6, the improved method outperforms the baseline method in most of the mirror points for the three test functions. The result shows the clear advantage of the improved method. As shown in Figure 6(a), in the case of test function 1, the accuracy of the improved method reaches the rounding error, resulting in some images not being displayed completely. It

demonstrates that the improved method has second-order accuracy and can reduce the error to less than the rounding error in the first-order test function. The accuracy of the improved method is much better than that of the incomplete linear interpolation. Figure 6(b-c) shows that the improved method is slightly worse than the baseline method when the mirror point is close to the fluid node. This is because the mirror point is too close to the fluid node, which reduces the error of incomplete linear interpolation and leads to the superiority of the baseline method over the improved method.

The typical incomplete linear interpolation model is shown in Figure 7. The value of the mirror point can be represented by the values of the three surrounding nodes as follows:

$$f(a_0) = \frac{(\Delta y - \Delta k) f(a_3)}{\Delta x} + \frac{\Delta k(\Delta x - \Delta h) f(a_1) + \Delta h \Delta k f(a_2)}{\Delta x^2} + R \quad (37)$$

where R is the error term, which is expressed as:

$$R = \frac{(\Delta y - \Delta k) f'_x(\Delta x - \Delta h)}{\Delta x} + o(\Delta x - \Delta h) + o(\Delta h) + o(\Delta y - \Delta k) + o(\Delta k) \quad (38)$$

Eq. (38) shows that the first term is the most significant source of error. As $\Delta k \to \Delta y$, the error becomes smaller, which is shown in Figure 6(b-c) where the error of the baseline method is significantly reduced at $Y = \Delta y$.

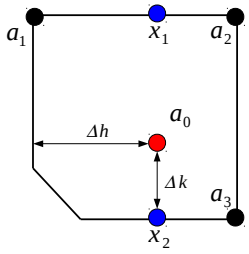

Figure 7: Incomplete linear interpolation model

In summary, this method has a significant advantage in efficiency compared to the other methods through unit tests. The improved method has better generality and scalability than the method proposed by Chi et al. [33]. The

improved method has second-order accuracy throughout and is capable of handling linear functions with only rounding errors. This method has significant advantages over the baseline method for different grid sizes and different mirror point locations. For most mirror point locations and grid sizes, the improved method had advantages over the other methods in accuracy.

3.2. Stationary rotating vortex

In order to verify the HBCGCM, a vortex problem with a theoretical solution is selected for testing. A circular boundary with a radius of R_G is employed in the current case, and the ghost-cell methods are used for the immersed boundary. Comparison of analytical and numerical solutions shows the accuracy of different boundary treatment methods. The counterclockwise rotation of the vortex is set in the initial flow field of the two-dimensional cylinder, as shown in Figure 8. For the following tests, the computational domain is set to $[0,1]\times[0,1]$.

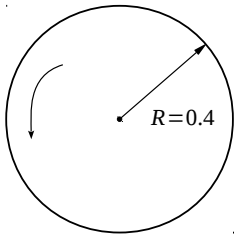

Figure 8: Stationary rotating vortex physics model

The initial parameters are set to:

$$x_c = 0.5, \quad y_c = 0.5, \quad R = 0.4, \quad t_{end} = 1, \quad \Delta h = \Delta x = \Delta y = \frac{1}{N}$$

The boundary is a circle around (x_c, y_c) with radius R . The reflective slip boundary condition is implemented at the immersed boundary.

The non-trivial radially symmetric and stationary solution is constructed by balancing hydrodynamic pressure and centripetal force per volume element:

$$\frac{d}{dr}p(r) = \rho(r)\frac{U(r)^2}{r} \tag{39}$$

where $U(r)$ denotes the velocity at distance r away from the origin. For $\rho_0 = 1$ the velocity field can be expressed as:

$$U(r) = \alpha \cdot \begin{cases} 2r/R & \text{if } 0 < r < R/2 \\ 2(1 - r/R) & \text{if } R/2 \leq r \leq R \\ 0 & \text{if } r > R \end{cases} \tag{40}$$

According to the boundary condition $p(R) = p_0 = 2$, the pressure distribution can be derived as follows:

$$p(r) = p_0 + 2\rho_0\alpha^2 \cdot \begin{cases} 2r^2/R^2 + 1 - ln2 & \text{if } 0 < r < R/2 \\ r^2/R^2 + 3 - 4r/R + ln(r/R) & \text{if } R/2 \leq r \leq R \\ 0 & \text{if } r > R \end{cases} \tag{41}$$

In Cartesian coordinates, physical quantities can be obtained from transformations into curvilinear coordinates:

$$\rho(x, y, t) = \rho_0,\ u(x, y, t) = -\sin\varphi U(r),\ v(x, y, t) = \cos\varphi U(r),\ p(x, y, t) = p(r) \tag{42}$$

where $r = \sqrt{(x - x_c)^2 + (y - y_c)^2}$, $\varphi = \arctan\frac{y-y_c}{x-x_c}$.

This exact smooth solution is applicable to measure the accuracy of immersed boundary methods by constructing a radially symmetric no-slip boundary around the origin. The error is chosen to be the $\|\varepsilon\|_2$ of the difference from the exact solution in the following tests.

~~To test the ability of the immersed boundary method to reproduce a uniform flow field in the non-trivial boundary case, the parameters of case 1 were chosen as:~~

~~$\alpha = 0, \quad R_G = R, \quad U_W = R\pi$~~

~~As shown in Figure , it can be seen that the HBCGCM is better than the rest of the methods in terms of density error and mass loss in the non-trivial boundary. Figure (a) clearly shows that the BCGCM enhances the accuracy of density respect to the baseline method. However, the L_2 norm of BCGCM does not differ significantly from the baseline method in mass loss in Figure (b). It demonstrates a lack of improvement for BCGCM in mass loss. The mean order~~

~~of the density error between HBCGCM, BCGCM and the baseline method can be calculated to be 1.79, 1.71 and 1.42, respectively. All of bilinear complete methods have higher order of the density error as opposed to the baseline method. This is because of the fact that incomplete bilinear interpolation is the most critical issue that causes the decreases of accuracy. Meanwhile, compared with the BCGCM, the result of HBCGCM shows higher error order. This could be largely explained by the fact that hybrid method use less ghost cell to project farther distance, compared with the BCGCM.~~

To test the immersed boundary method in the case of almost no boundary interactions, the parameters of case 1 are chosen as:

$$\alpha = R\pi, \quad R_G = R$$

It can be seen that HBCGCM can achieve more accurate results by comparing with BCGCM and baseline GCM in Figure 9. As shown in Figure 9 (a), the advantages of HBCGCM become increasingly conspicuous with the decrease of grids size. It can be seen from Figure 9 (b) that on the coarse grid, HBCGCM can obtain a lower $\|\varepsilon\|_1$. As the grid size decreases, the $\|\varepsilon\|_1$ of the three GCM methods gradually tends to the same smaller value. With decreasing grids size the gap between the BCGCM and the baseline GCM results are successively closed in Figure 9 (c), while for the coarse grids simulation, the HBCGCM and BCGCM are almost consistent with each other. Compared with other methods, the baseline GCM has a larger error, which makes $\|\varepsilon\|_\infty$ larger, as shown in Figure 9 (d). In the case of the coarse grid $N = 20$, there are greater fluctuations in physical quantities near the boundary and the incomplete linear interpolation in the baseline GCM will result in a greater loss of accuracy. Therefore, the $\|\varepsilon\|_2$ of the HBCGCM and BCGCM under the coarse grid will be better than that of the baseline GCM.

To test the effectiveness of the immersed boundary method in the case of very strong shear flow, the immersed boundary is placed precisely at the point of maximum shear flow velocity in case 2, i.e.

$$\alpha = R\pi, \quad R_G = R/2$$

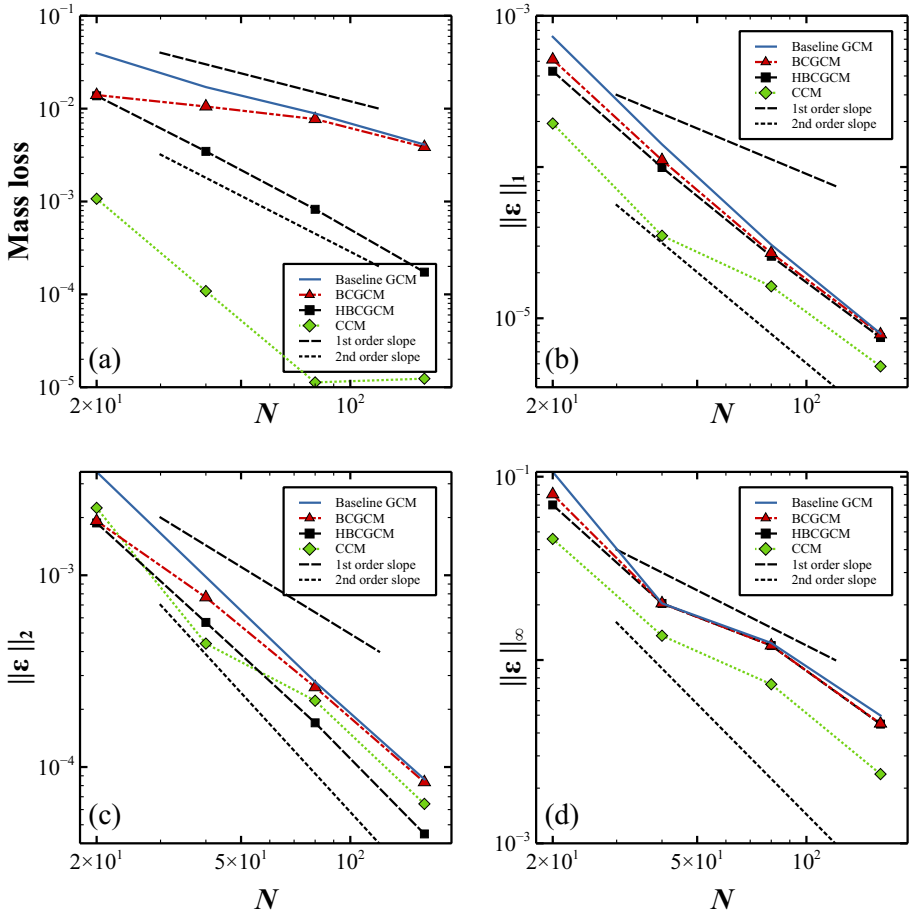

Figure 9: Comparison of three methods in the no boundary interactions case, (a) Mass loss (b) $\|\varepsilon\|_1$ of density (c) $\|\varepsilon\|_2$ of density (d) $\|\varepsilon\|_\infty$ of density

As shown in Figure 10, the baseline method is the worst method with the worst accuracy. The HBCGCM presents the lowest error among all GCM methods in terms of mass loss. This indicates that the HBCGCM has higher convergence than the CCM. Compared with BCGCM and baseline GCM, HBCGCM can obtain a lower $\|\varepsilon\|_1$, as shown in Figure 10 (b). Nevertheless, the advantage of the HBCGCM relative to the BCGCM is not fully realized in $\|\varepsilon\|_2$.

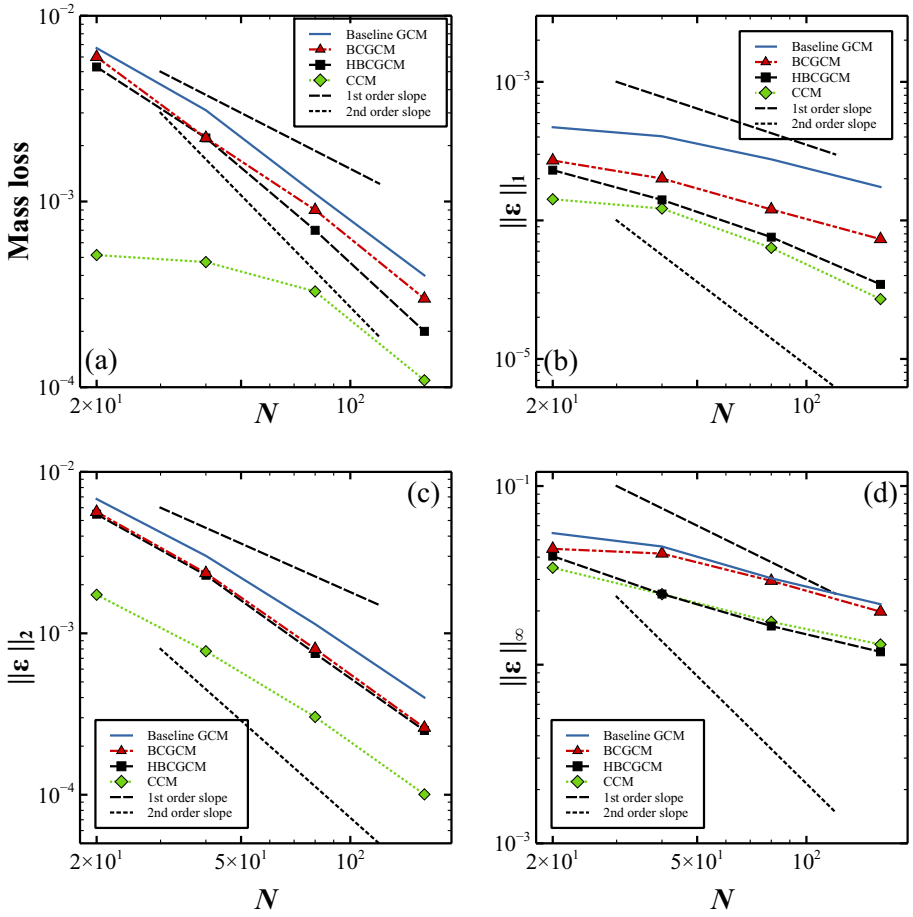

Figure 10: Comparison of three methods in the strong shear flow case, (a) Mass loss (b) $\|\varepsilon\|_1$ of density (c) $\|\varepsilon\|_2$ of density (d) $\|\varepsilon\|_\infty$ of density

Strong shear flow is obtained by decreasing the radius of the computational domain. The size of the grid relative to the boundary radius increases as the boundary radius decreases. Based on previous analysis, when the physical quantities of surrounding grids change drastically, the difference in the error of the HBCGCM and the BCGCM is not very significant. If more significant differences are required, then one would have to set finer grids in this case. As the

grid size gradually decreases, HBCGCM can obtain the lowest $\|\varepsilon\|_\infty$ compared with other methods, as shown in Figure 10(d). A smaller $\|\varepsilon\|_\infty$ indicates that HBCGCM has a smaller upper limit of error when dealing with larger gradients of physical quantities.

~~The HBCGCM has significant advantages over the other methods for boundary treatment. In addition, since each case is set for the different parameters, according to its type of boundary, the error is not identical. The smallest error is obtained by using HBCGCM in case 2. First, in case 1, primitive variables of ghost cells reset when the boundary is rotatable, and the resetting causes a loss of accuracy. While in case 3, the primitive variables around the image point and the extrapolation point change drastically in strong shear flow.~~

As shown in Figures 9-10, the HBCGCM has higher accuracy and convergence in all GCM. The simulation results using CCM have a smaller mass loss because the CCM method has higher conservation. However, the convergence of the mass loss of the CCM method is worse than that of HBCGCM, especially at the boundary with the strong shear flow. At the same time, a significant trend is that as the grid size decreases, the error of HBCGCM decreases closer to CCM. This shows that HBCGCM has higher convergence than CCM. Considering the complexity of the CCM in boundary treatment and the larger computational cost (discussion in Sec 3.7), HBCGCM is considered to be more attractive.

The HBCGCM has significant advantages over the other GCMs for boundary treatment. In addition, since each case is set for different parameters, the error is not identical according to its type of boundary. The smallest error is obtained by using HBCGCM in case 1. While in case 2, the primitive variables around the image point and the extrapolation point change drastically in strong shear flow. As discussed above, extrapolation with primitive variables, which change drastically, may lead to incorrect conclusions.

These cases demonstrate the significant advantages of the HBCGCM for different boundary types including no boundary interactions and boundary in shear flow. In these cases, the HBCGCM consistently performed better than the other GCM, particularly when compared in terms of mass loss. Meanwhile, with

411 the reduction of the grids size, it can be easier to demonstrate the advantages
412 of the HBCGCM over other GCMs.

413 *3.3. Prandtl-Meyer expansion*

The cases of Prandtl-Meyer expansion wave can be quantitatively verified by the immersed boundary method [33, 28, 48] because of its analytical solution. The steady-state problem of smooth flow has a constant entropy, whose value is $S = p/\rho^{\gamma}$. When the fluid Mach number is expanded from Ma_1 to Ma_2 by the expansion wave, the deflection angle can be calculated as follows:

$$\begin{aligned}\theta = &\left[\sqrt{\frac{\gamma+1}{\gamma-1}}\arctan\sqrt{\frac{\gamma-1}{\gamma+1}(\mathrm{Ma}_2^2-1)} - \arctan\sqrt{\mathrm{Ma}_2^2-1}\right] - \\ &\left[\sqrt{\frac{\gamma+1}{\gamma-1}}\arctan\sqrt{\frac{\gamma-1}{\gamma+1}(\mathrm{Ma}_1^2-1)} - \arctan\sqrt{\mathrm{Ma}_1^2-1}\right]\end{aligned} \tag{43}$$

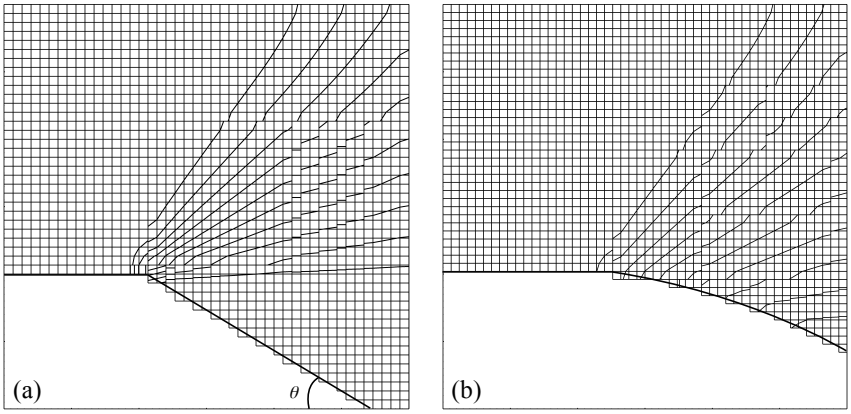

Figure 11: Density contours obtained from the computation of a Prandtl-Meyer expansion wave at Mach 1.2, (a) Prandtl-Meyer expansion wave case with the straight boundary (b) Prandtl-Meyer expansion wave case with the curved boundary

414 The Prandtl-Meyer expansion wave case with the straight wall surface is
415 calculated to compare the convergence of entropy results calculated by different
416 methods. The convergence of entropy is compared for the cases of 20°, 30°, 40°
417 and 50° deflection angles θ, as shown in Figure 11(a). An accuracy study of the
418 algorithm is performed for this problem by conducting a series of calculations
419 on grids of varying resolution: 600×600, 300×300, 150×150, 60×60, 30×30.

Figure 12 shows the $\|\varepsilon\|_2$ of entropy in the vicinity of the boundary with grid size for the different methods. It can be seen that in all cases the HBCGCM yields better performance in convergence. Although the overall performance of BCGCM is better than the baseline method, the improvement is only maximally 37% compared to the baseline method.

Table 1: The order of convergence in the $\|\varepsilon\|_2$, where r_2^B, r_2^G and r_2^H represent orders of Baseline GCM, BCGCM and HBCGCM, respectively

Angle	r_2^B	r_2^G	r_2^H
20°	1.25	1.25	1.36
30°	1.13	1.21	1.37
40°	1.17	1.20	1.35
50°	1.16	1.16	1.33

Table 1 summarizes the convergence orders for the Prandtl-Meyer expansion cases. The results for entropy suggest that the order of accuracy of the discretization over the ghost-cells (viz., in the vicinity of the boundary) is $r_2^H \approx 1.35$, which is a clear improvement when compared to other immersed boundary methods, where $r_2 \approx 1.14$ was reported by Pember et.al. [49]. Although certain studies [28, 48] reported better conservation, note that this was obtained using a conservation-based cut-cell method.

It is worth noting that the Mach number after the expansion waves is independent of the expansion process and depends only on the total deflection angle. The Prandtl-Meyer expansion wave case with a curved boundary can be set, as shown in Figure 11(b). The geometry used for expansion wave is set according to the used by Berger and LeVeque [50]. For the convenience of calculation, the computational domain is set to $[-1, 2] \times [-1, 2]$, and the turning point of the

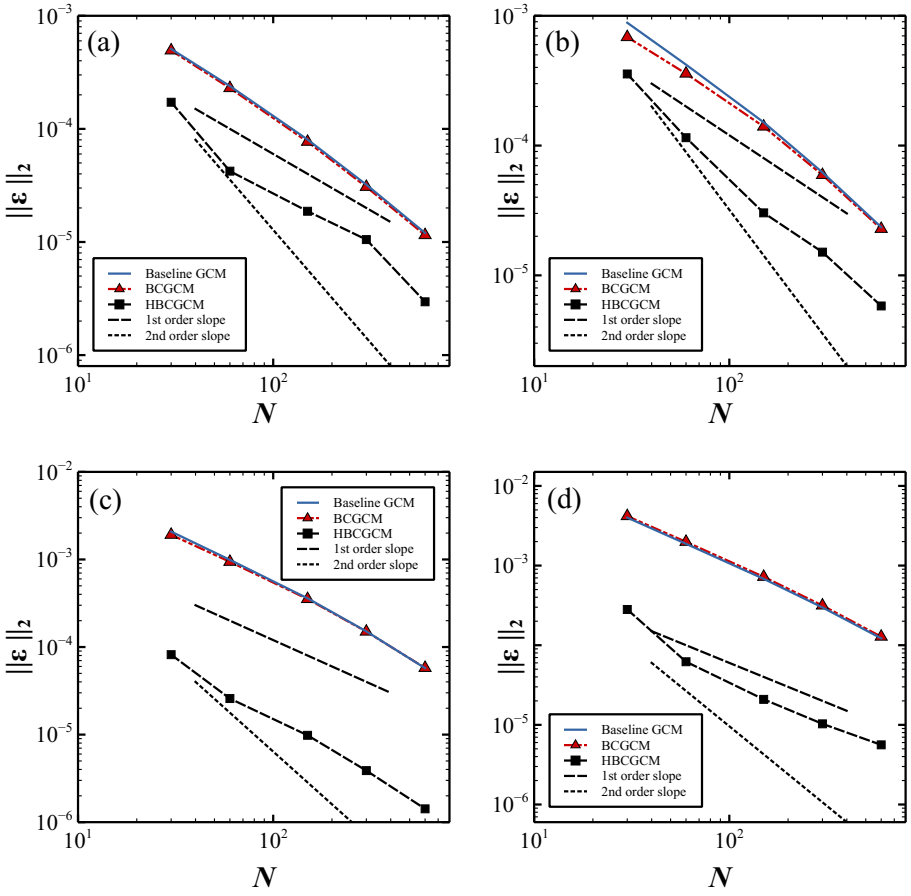

Figure 12: Variation of $\|\varepsilon\|_2$ with grid size for different deflection angles, (a) 20° (b) 30° (c) 40° (d) 50°

boundary is set to $(0, 0)$. The curved boundary is given by the function:

$$y(x) = \begin{cases} 0 & x \leqslant 0 \\ 0.3x^2 & 0 \leqslant x \leqslant 0.6 \\ 0.108 - 0.36(x - 0.6) & x \geqslant 0.7 \end{cases} \tag{44}$$

The grid size is set to $N = 150$. Because the analytical solution of Mach number is known, the relative error of the simulation results can be calculated as follows:

$$e_R = \frac{|\mathrm{Ma}_{exact} - \mathrm{Ma}_{simulation}|}{\mathrm{Ma}_{exact}}. \tag{45}$$

The relative error of Mach number with different methods is shown in Figure 13. It is found that the error curve is not smooth in Figure 13. This might be due to the way the boundary values are calculated. The physical quantities of the fluid in the calculation are stored at the central node, and the node is not exactly on the boundary. The central node close enough to the boundary is selected according to the threshold value $\Delta x/10$, and then mapped to the boundary by Mach lines. The HBCGCM yielded the highest precision value in the method shown in Figure 13. Meanwhile, a relatively substantial improvement by using BCGCM is exhibited, compared to the baseline method. The BCGCM and baseline method have comparable performance at the large deflection angle, but at the small deflection angle the BCGCM gains about 5 to 100 times improvement in accuracy with the baseline method. It is noteworthy that the relative errors of the BCGCM and baseline method also increase as the deflection angle increases. Nevertheless, the larger angle seemed to have a negligible influence on the accuracy of HBCGCM. The overall accuracy of HBCGCM illustrated the excellent capability of this method to handle the curved boundary.

The $\|\varepsilon\|_2$ for the solution error of the entropy in the vicinity of the boundary are calculated as 1.01×10^{-4}, 8.78×10^{-5} and 2.32×10^{-5} corresponding to the baseline method, BCGCM and HBCGCM, respectively. The HBCGCM indicates that its $\|\varepsilon\|_2$ is more than four times lower than that of the baseline method. From the above results, the HBCGCM improves the accuracy overall and yields better convergence. The Prandtl-Meyer expansion wave cases cover the different type of boundaries. Both the results of straight boundaries and curved boundaries show that HBCGCM performed better. Thus, the above conclusions can be extended to other cases. The HBCGCM is considered to have significant advantages over other methods in compressible flow simulations.

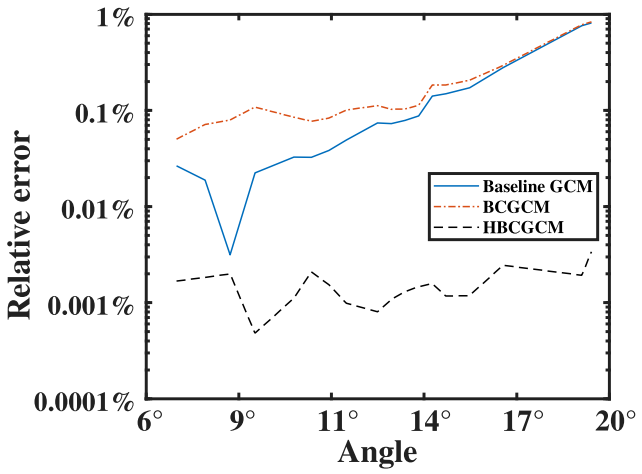

Figure 13: Comparisons of Mach number relative error versus deflection angle for different methods at $N = 150$.

3.4. Double Mach reflection

This case concerns the simulation of the interaction of a two-dimensional shock wave with a wedge using HBCGCM. This test problem has been widely used to verify numerical methods [51]. The experimental results by driving a shock down a tube, which contains a wedge, can be found in the previous work [52]. A planar two-dimensional shock wave in air impinges on a ramp inserted into the shocktube at angle $\alpha = 36^\circ$ and creates a growing transitional Mach reflection pattern. The ramp is treated by an immersed boundary method as described in the previous section.

The shock tube is filled with air ($\gamma = 1.4$) at rest ($u_{1,0} = u_{2,0} = 0$) at ambient temperature ($300K$) and ambient pressure $P_0 = 2kPa$, leading to a density of $\rho_0 = 0.02312kg/m^3$and speed of sound $c_0 = 348.04m/s$. The shock wave travels at Mach number $Ma = 4.5$, which leads to the constant state $\rho_s = 0.11123kg/m^3$, $u_{n,s} = 1566.2m/s$, $u_{t,s} = 0$, and $P_s = 46.917kPa$ behind the shock. Herein, $u_{n,s}$ and $u_{t,s}$ denote the component of the velocity vector normal and tangential to the shock front, respectively. The computational domain $[-5mm, 70mm] \times [0, 60mm]$ is employed for the simulations with im-

mersed boundary. The shock front is initially located at $(0, 0)$ with the shock propagating to the right. This case adopts constant inflow boundary conditions at the left boundary, reflective slip wall boundary conditions at the bottom, and outflow boundary conditions elsewhere. 6000×4800 cells are employed in different boundary treatment methods which results in $\Delta x = \Delta y = 12.5 \mu m$.

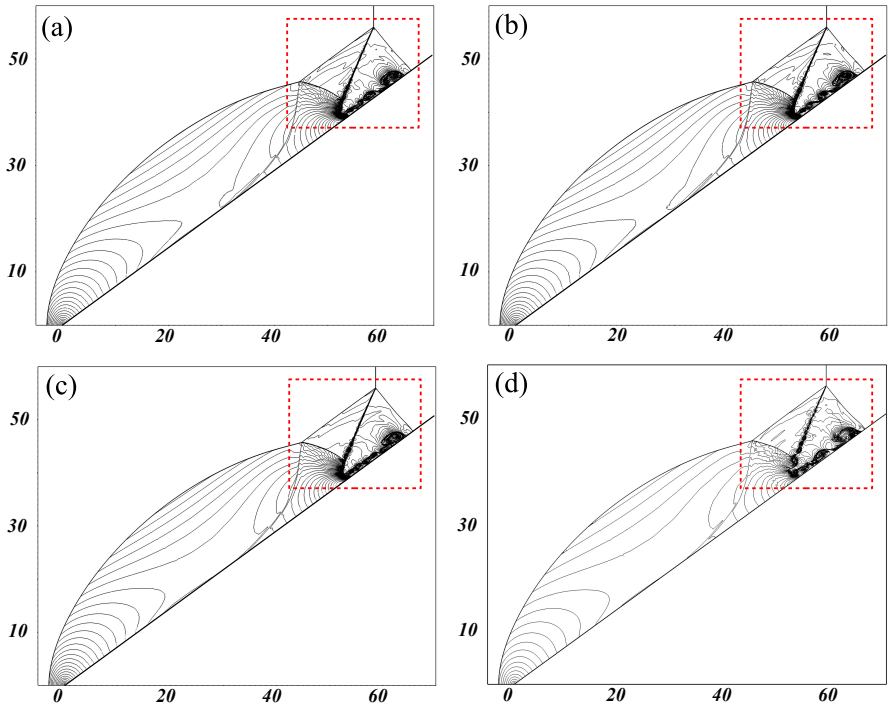

Figure 14: Counters of density ,(a) Baseline GCM (b) BCGCM (c) HBCGCM (d) CCM

The results at $t_{end} = 40 \mu s$ are shown in Fig 14. The moving shocks and Mach stems relative to the solid boundaries are identical in the four methods. This indicates that all discontinuities are predicted at the same locations in a fine grid. The differences between the four methods are represented in the jet structure developed along the ramp wall. An enlargement of just the jet structure which labeled by dash line in Fig 14 is shown in Fig 15. A Kelvin-Helmholtz instability can be observed from the vortices along the slip line (labeled by dash line in Fig 15). It is generally thought that a change of the numerical scheme

has larger influence on the K-H instability than utilizing different immersed boundary methods [37]. In both methods, the leading edge of the jet intersects the boundary at a right angle, which is considered a physically correct result. The smaller-scale vortices occur in the slip line and jet structures by using the improved method. At the same time, compared with the CCM method, the improved GCM method has a smoother physical quantity distribution.

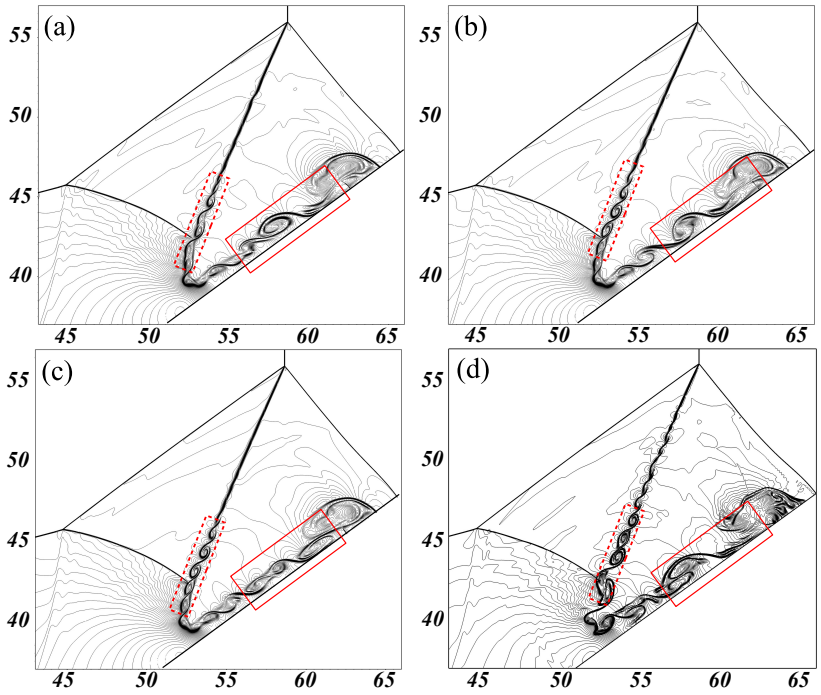

Figure 15: Enlargement of the Mach reflection pattern ,(a) Baseline GCM (b) BCGCM (c) HBCGCM (d) CCM

The simulation using the baseline method on a 6000×4800 grid is adopted as an "exact" solution for quantitative analysis [49]. The lower resolution results on a 1500×1200 grid are adopted to calculate density errors $\|\varepsilon\|$ with the "exact" solution. The density errors of the total computational domain and the domain near the boundary are presented in Table 2. The results suggest that

Table 2: Result of density errors for double Mach reflection case

Method	$\|\varepsilon\|_1$		$\|\varepsilon\|_2$		$\|\varepsilon\|_\infty$	
	total	boundary	total	boundary	total	boundary
Baseline GCM	7.2×10^{-4}	0.0030	0.0049	0.011	0.12	0.10
BCGCM	2.5×10^{-4}	6.2×10^{-4}	0.0021	0.0024	0.074	0.047
HBCGCM	2.3×10^{-4}	5.0×10^{-4}	0.0020	0.0018	0.072	0.044
CCM	4.2×10^{-4}	0.0021	0.0040	0.010	0.25	0.25

the simulation using HBCGCM has lower error in $\|\varepsilon\|_1$, $\|\varepsilon\|_2$ and $\|\varepsilon\|_\infty$.

3.5. Moving-shock/obstacle interaction

This case concerns the simulation of the interaction of a moving-shock shock wave with a sharp wedge using HBCGCM. In this case, a moving-shock impinges on a wedge obstacle. As time evolves, the interaction produces complicated flow patterns. The numerical setting follows the experiments of Chang et.al [53]. The ambient temperature is set to $300K$, and the ambient pressure is set to $50kPa$. The flow field is initialized with the Rankine-Hugoniot conditions, and the Mach number of a moving-shock (marked in red in Figure 16) is set to 1.34. For the simulations with immersed boundary, the computational domain $L_x \times L_y = 190mm \times 115mm$ is employed. The obstacle is set as an equilateral triangle with a side length of $20mm$, where a no-slip wall boundary condition is adopted. The 3800×2300 grids are employed which $\Delta x = \Delta y = 50\mu m$ and the CFL number is set equal to 0.5. This case adopts constant inflow boundary conditions at the left boundary, reflective slip wall boundary conditions at the bottom and top, and outflow boundary conditions at the right boundary.

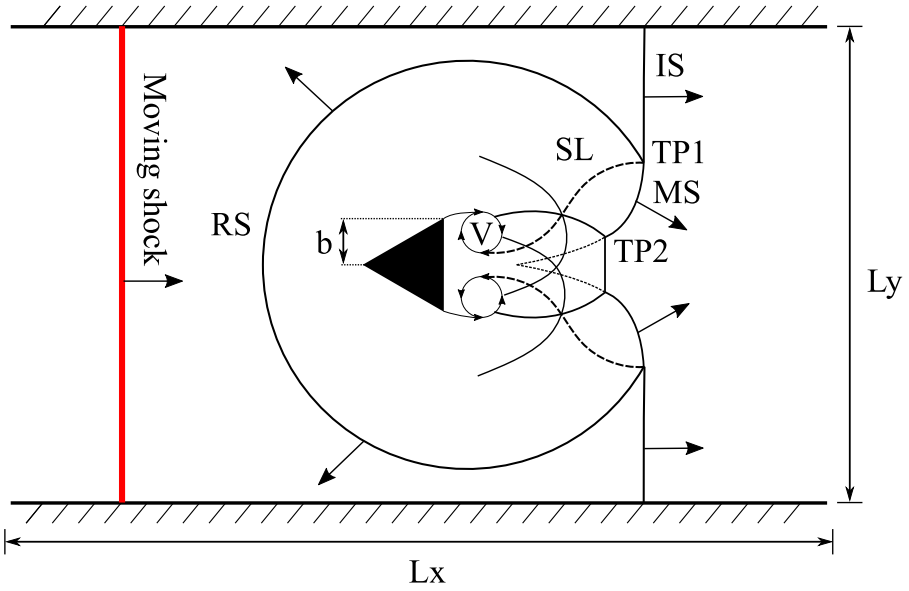

Figure 16: Configuration of Schardin's problem and schematic diagram of shock–vortex interaction. RS: reflected shock, IS: incident shock, SL: slip line, MS: Mach stem, TP: triple point and V:vortex

Some flow characteristics can be highlighted, consisting of multiple Mach stems, triple points, reflected shocks, slip-lines and vortices (a detailed description of the flow field has been given by Chang et al. [53]). The density schlieren calculated by the HBCGCM is compared with experimental results, as shown in Figure 17.

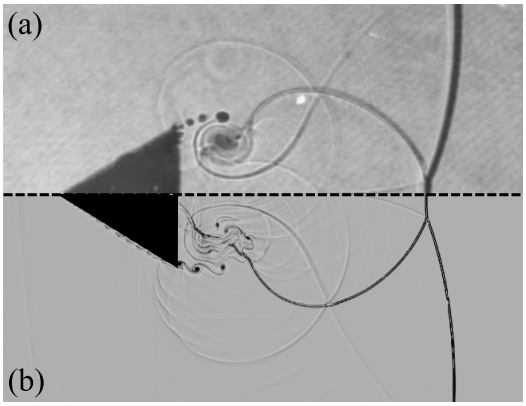

Figure 17: Density schlieren of shock-vortex interaction at $t = 128\mu s$, (a) the experimental results of Chang et.al [53] (b) the results of simulation by using the HBCGCM

It can be seen that the results of the HBCGCM are consistent with the experiment in Figure 17 , and the flow field is consistent with that described in Figure 16.

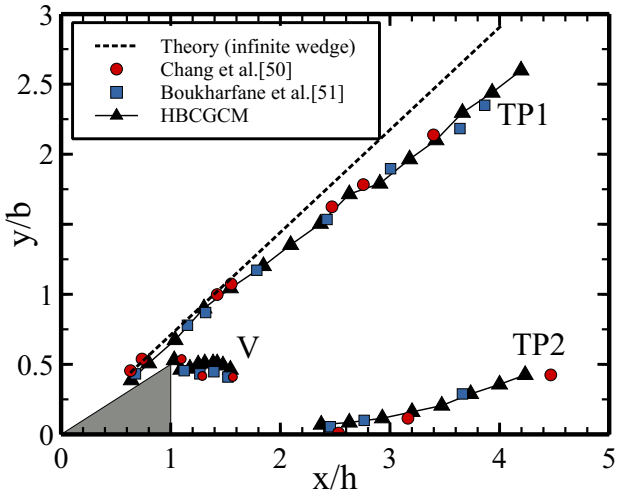

Figure 18: Comparison of triple point (TP1 & TP2) trajectory and locus of vortex center (V). h is the wedge height while $b = h \cdot tan(\pi/3)$ is the edge length.

The HBCGCM results are compared with the experimental data of Chang et al. [53], a theoretical solution from ray-shock theory and the numerical

simulations of Boukharfane et al. [54], as shown in Figure 18. The comparison is conducted in terms of triple point trajectory and locus of vortex center. The simulated evolution of the two triple point (TP1 & TP2) trajectory and the locus of vortex center (V) by HBCGCM agree well with previous numerical and experimental results. This demonstrates that the HBCGCM has the ability to capture flow field characteristics well even when the boundary interface is sharp.

3.6. Blunt body shock-induced combustion

The case of blunt body shock-induced combustion with an internal boundary is employed to demonstrate the capability and accuracy of the HBCGCM. The bow shock of a hypersonic blunt body can induce oscillatory combustion of combustible mixtures [55]. This case has a complex geometric boundary, and a violent chemical reaction zone exists near the boundary.

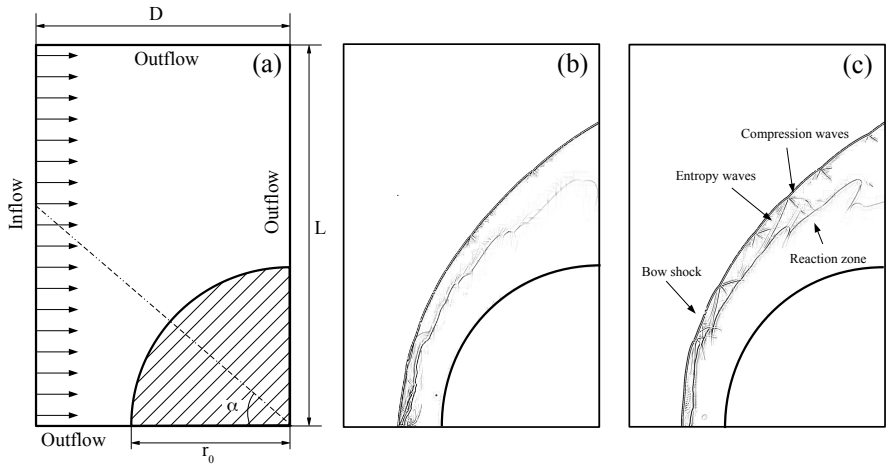

Figure 19: Density schlieren of the blunt projectile at $t = 40\mu s$, (a) physical model (b) Baseline method (c) HBCGCM

As shown in Figure 19(a), a blunt projectile is set in the computational domain, and the rest of the computational domain is set to the $H_2 : O_2 : N_2$ mixture (molar ratio of $H_2 : O_2 : N_2 = 2 : 1 : 3.76$). The initial temperature of the combustible mixture is $298K$, and the initial pressure is $42.663kPa$. The

blunt projectile velocity is $1931m/s$, which is the same as the CJ velocity of the detonation. The length of the computational domain is $L = 18mm$, the width is $D = 12mm$, and the radius of the blunt projectile is $r_0 = 7.5mm$. The left boundary condition is set to inflow condition, and the wall is processed with no-slip boundary condition by HBCGCM. In this case, the Riemann solver uses the HLL Riemann solver which proposed by the Harten, Lax, and Van Leer [56]. A detailed H_2 / air reaction model is adopted with 12 species and 42 elementary reactions [57]. The 1920×2880 cells are employed in different boundary treatment methods where $\Delta x = \Delta y = 6.25\mu m$.

The oscillation frequency of the pressure simulated by the baseline GCM is $707.2kHz$, and that affected by the HBCGCM is $714.8kHz$. According to Lehr et al. [55], the pressure oscillation frequency is $725kHz$. The error of the baseline method result is 2.5%, and the error of the improved method result is 1.4%. The density schlieren calculated by the two different methods were compared, as shown in Figure 19. Figure 19 (b-c) shows significant differences in the flow field between the bow shock and the combustion surface. With the HBCGCM, a significant alternation of entropy waves and compression waves between the bow shock wave and the combustion front is observed. This alternating wave structure is the typical structure of supersonic blunt projectile [58], but it is not obtained in the baseline GCM. Based on the above results, it can be concluded that the HBCGCM is convergent and stable. The use of the HBCGCM in the current case can obtain results that are more consistent with the experimental phenomena.

3.7. CPU time comparison

CPU time is an easily available indicator of numerical simulations, an indirect estimator of resource consumption and efficiency. The BCGCM has an additional interpolation/extrapolation operation compared to the baseline method. Compared with the BCGCM, the HBCGCM requires an additional judgment procedure to select the method suitable for the specific ghost-cell. From the above work, it can be concluded that the HBCGCM has some signif-

icant advantages in terms of accuracy in compressible flow problems. However, if the baseline method is to be replaced, then the computational efficiency of the HBCGCM or BCGCM must be within acceptable limits. It is necessary to evaluate the time spent on boundary processing by the HBCGCM and BCGCM versus the baseline method. The computational cost of the CCM method has also been added for comparison to make the conclusion more convincing. The CPU time has been measured through simulations with a single core CPU for the stationary rotating vortex cases 1 & 2 with $N = 160$ and dimensionless physical time $t = 1$. The parameters of Prandtl-Meyer expansion case are set as $N = 600$ and physical time $t = 0.03s$. The parameters of double Mach reflection case are set as $N_x \times N_y = 1500 \times 1200$ and physical time $t = 4 \times 10^{-5}s$.

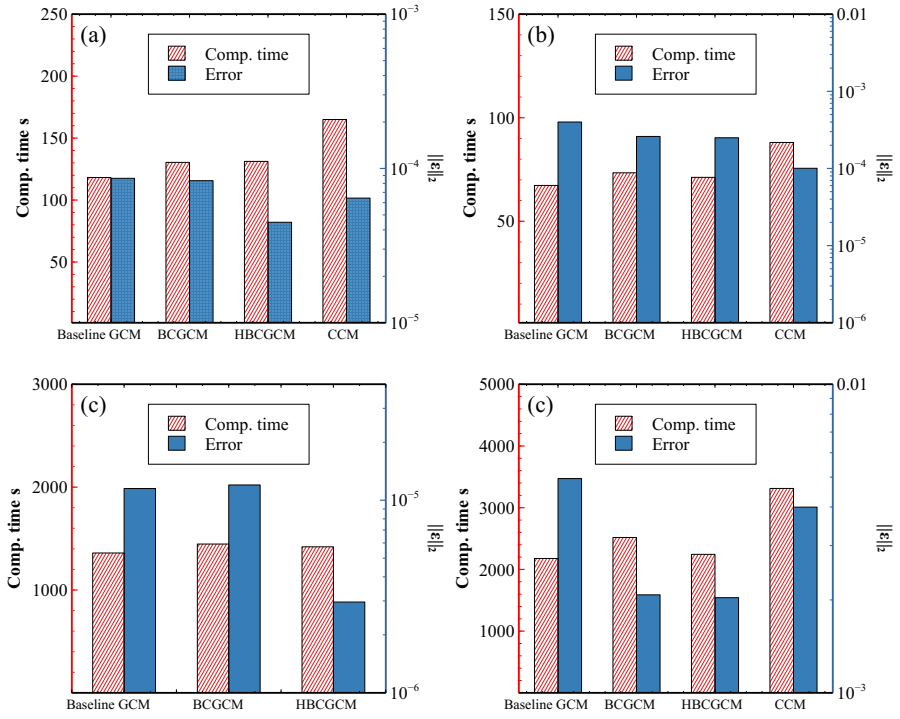

Figure 20: The CPU time and accuracy comparison, (a) Stationary rotating vortex case 1 (b) Stationary rotating vortex case 2 (c) Prandtl-Meyer expansion (d) Double Mach reflection

~~The additional computational cost of the HBCGCM is negligible compared to the baseline method. Although there are additional judgments using HBCGCM, not all ghost cells require additional extrapolation. Consequently, the HBCGCM is shown to be less costly and more cost-effective than the BCGCM. As can be seen from Table , in the stationary rotating vortex case, the computational cost of HBCGCM is 8.7% higher than that of BCGCM. However, in the Prandtl-Meyer expansion case, the HBCGCM has a lower computational cost. It can be considered that the HBCGCM with high precision is the better choice based on the efficiency.~~

Figure 20 shows that the computational costs of the HBCGCM, BCGCM, baseline method and CCM. It is evident that the CPU time using CCM is much longer than that using the GCM method, but the accuracy of CCM is lower than HBCGCM. The additional computational cost of the HBCGCM is negligible compared to the baseline method. Although there are additional judgments using HBCGCM, not all ghost-cells require additional extrapolation. On the other hand, the accuracy of HBCGCM is sufficiently higher than the baseline method. Consequently, the HBCGCM is shown to be less costly and more cost-effective than the BCGCM. It can be considered that the HBCGCM with high precision is the better choice based on efficiency.

4. Conclusions

This paper proposes a hybrid bilinearly complete, globally second-order-accurate ghost-cell method that can be applied with compressible flows. Based on the previous studies, an analytical second-order accurate reconstruction method for the ghost-cell is proposed. The unit test shows that on smooth given functions second-order accuracy is maintained, and it has a significant improvement over the previous method. Through the hybrid implementation with the baseline method, a further increase in the accuracy of the improved reconstruction method is achieved.

The results from the symmetric circular boundary (stationary vortex cases)

show the accuracy of HBCGCM is higher than that of the remaining methods. By testing the Prandtl-Meyer expansion cases, the HBCGCM is found to have significant advantages in compressible flow. For problems with shocks, the HBCGCM is considered to have the capability and stability to handle problems with discontinuities. For problems with a sharp interface, the HBCGCM has the ability to capture field characteristics. Finally, the cases of shock-induced combustion also demonstrate that the HBCGCM also performs well in problems with chemical reactions. The HBCGCM with higher accuracy can ensure the efficiency of the calculation by comparing the calculation time.

It should be straightforward to apply the HBCGCM to three-dimensional compressible flow simulations. The level-set methods can represent the three-dimensional boundary easily. The reconstruction method can be used along the boundary normal, and the mirror point and the extrapolation point can use the surrounding nodes for trilinear interpolation. The implementation of the HBCGCM in three-dimensional simulations has already started. Future work will also include the combination of HBCGCM and adaptive mesh refinement to reduce the amount of mesh required for three-dimensional simulations.

Acknowledgments

This work is supported by the National Natural Science Foundation of China (No. 11702323). Thanks are due to Siqi Hu and Ke Zhu for support in writing the paper.

References

[1] C. S. Peskin, Flow patterns around heart valves: a numerical method, Journal of computational physics 10 (2) (1972) 252–271.

[2] C. S. Peskin, Numerical analysis of blood flow in the heart, Journal of computational physics 25 (3) (1977) 220–252.

[3] C. S. Peskin, The immersed boundary method, Acta numerica 11 (2002) 479–517.

[4] R. Mittal, G. Iaccarino, Immersed boundary methods, Annu. Rev. Fluid Mech. 37 (2005) 239–261.

[5] D. K. Clarke, M. Salas, H. Hassan, Euler calculations for multielement airfoils using cartesian grids, AIAA journal 24 (3) (1986) 353–358.

[6] H. S. Udaykumar, W. Shyy, M. M. Rao, Elafint: a mixed eulerian–lagrangian method for fluid flows with complex and moving boundaries, International journal for numerical methods in fluids 22 (8) (1996) 691–712.

[7] T. Ye, R. Mittal, H. Udaykumar, W. Shyy, An accurate cartesian grid method for viscous incompressible flows with complex immersed boundaries, Journal of computational physics 156 (2) (1999) 209–240.

[8] J. Mohd-Yusof, Combined immersed-boundary/b-spline methods for simulations of flow in complex geometries, Center for turbulence research annual research briefs 161 (1) (1997) 317–327.

[9] E. Fadlun, R. Verzicco, P. Orlandi, J. Mohd-Yusof, Combined immersed-boundary finite-difference methods for three-dimensional complex flow simulations, Journal of computational physics 161 (1) (2000) 35–60.

[10] Y.-H. Tseng, J. H. Ferziger, A ghost-cell immersed boundary method for flow in complex geometry, Journal of computational physics 192 (2) (2003) 593–623.

[11] H. Ding, C. Shu, Q. Cai, Applications of stencil-adaptive finite difference method to incompressible viscous flows with curved boundary, Computers & fluids 36 (4) (2007) 786–793.

[12] H. Luo, R. Mittal, X. Zheng, S. A. Bielamowicz, R. J. Walsh, J. K. Hahn, An immersed-boundary method for flow–structure interaction in biological

systems with application to phonation, Journal of computational physics 227 (22) (2008) 9303–9332.

[13] J. H. Seo, R. Mittal, A high-order immersed boundary method for acoustic wave scattering and low-mach number flow-induced sound in complex geometries, Journal of computational physics 230 (4) (2011) 1000–1019.

[14] J. Xia, K. Luo, J. Fan, A ghost-cell based high-order immersed boundary method for inter-phase heat transfer simulation, International Journal of Heat and Mass Transfer 75 (2014) 302–312.

[15] K. Luo, Z. Zhuang, J. Fan, N. E. L. Haugen, A ghost-cell immersed boundary method for simulations of heat transfer in compressible flows under different boundary conditions, International Journal of Heat and Mass Transfer 92 (2016) 708–717.

[16] J. H. Ferziger, M. Perić, R. L. Street, Computational methods for fluid dynamics, Vol. 3, Springer, 2002.

[17] S. Majumdar, G. Iaccarino, P. Durbin, et al., Rans solvers with adaptive structured boundary non-conforming grids, Annual Research Briefs 1.

[18] F. N. Felten, T. S. Lund, Kinetic energy conservation issues associated with the collocated mesh scheme for incompressible flow, Journal of Computational Physics 215 (2) (2006) 465–484.

[19] D. Pan, T.-T. Shen, Computation of incompressible flows with immersed bodies by a simple ghost cell method, International journal for numerical methods in fluids 60 (12) (2009) 1378–1401.

[20] D. Pan, C.-H. Chang, The capturing of free surfaces in incompressible multi-fluid flows, International Journal for Numerical Methods in Fluids 33 (2) (2000) 203–222.

[21] D. Pan, An immersed boundary method on unstructured cartesian meshes for incompressible flows with heat transfer, Numerical Heat Transfer, Part B: Fundamentals 49 (3) (2006) 277–297.

[22] A. Gilmanov, F. Sotiropoulos, A hybrid cartesian/immersed boundary method for simulating flows with 3d, geometrically complex, moving bodies, Journal of computational physics 207 (2) (2005) 457–492.

[23] A. Gilmanov, S. Acharya, A computational strategy for simulating heat transfer and flow past deformable objects, International Journal of Heat and Mass Transfer 51 (17-18) (2008) 4415–4426.

[24] M. Shrivastava, A. Agrawal, A. Sharma, A novel level set-based immersed-boundary method for cfd simulation of moving-boundary problems, Numerical Heat Transfer, Part B: Fundamentals 63 (4) (2013) 304–326.

[25] R. Mittal, H. Dong, M. Bozkurttas, F. Najjar, A. Vargas, A. Von Loebbecke, A versatile sharp interface immersed boundary method for incompressible flows with complex boundaries, Journal of computational physics 227 (10) (2008) 4825–4852.

[26] P. A. Berthelsen, O. M. Faltinsen, A local directional ghost cell approach for incompressible viscous flow problems with irregular boundaries, Journal of computational physics 227 (9) (2008) 4354–4397.

[27] R. Ghias, R. Mittal, H. Dong, A sharp interface immersed boundary method for compressible viscous flows, Journal of Computational Physics 225 (1) (2007) 528–553.

[28] H. Ji, F.-S. Lien, E. Yee, Numerical simulation of detonation using an adaptive cartesian cut-cell method combined with a cell-merging technique, Computers & fluids 39 (6) (2010) 1041–1057.

[29] R. Deiterding, Parallel adaptive simulation of multi-dimensional detonation structures, Dissertation. de, 2003.

[30] R. Deiterding, A parallel adaptive method for simulating shock-induced combustion with detailed chemical kinetics in complex domains, Computers & Structures 87 (11-12) (2009) 769–783.

[31] R. Deiterding, F. Cirak, S. P. Mauch, D. Meiron, A virtual test facility for simulating detonation-and shock-induced deformation and fracture of thin flexible shells, International Journal for Multiscale Computational Engineering 5 (1).

[32] R. Deiterding, R. Radovitzky, S. P. Mauch, L. Noels, J. C. Cummings, D. I. Meiron, A virtual test facility for the efficient simulation of solid material response under strong shock and detonation wave loading, Engineering with Computers 22 (3-4) (2006) 325–347.

[33] C. Chi, B. J. Lee, H. G. Im, An improved ghost-cell immersed boundary method for compressible flow simulations, International Journal for Numerical Methods in Fluids 83 (2) (2017) 132–148.

[34] C. Chi, A. Abdelsamie, D. Thévenin, A directional ghost-cell immersed boundary method for incompressible flows, Journal of Computational Physics 404 (2020) 109122.

[35] R. Deiterding, Amroc-blockstructured adaptive mesh refinement in object-oriented c++ (2003).

[36] R. Deiterding, Construction and application of an amr algorithm for distributed memory computers, in: Adaptive Mesh Refinement-Theory and Applications, Springer, 2005, pp. 361–372.

[37] R. Deiterding, Block-structured adaptive mesh refinement-theory, implementation and application, in: Esaim: Proceedings, Vol. 34, EDP Sciences, 2011, pp. 97–150.

[38] W. Zhang, A. Almgren, V. Beckner, J. Bell, J. Blaschke, C. Chan, M. Day, B. Friesen, K. Gott, D. Graves, M. Katz, A. Myers, T. Nguyen, A. Nonaka, M. Rosso, S. Williams, M. Zingale, AMReX: a framework for block-structured adaptive mesh refinement, Journal of Open Source Software 4 (37) (2019) 1370.

[39] E. F. Toro, Riemann solvers and numerical methods for fluid dynamics: a practical introduction, Springer Science & Business Media, 2013.

[40] B. Van Leer, Towards the ultimate conservative difference scheme. v. a second-order sequel to godunov's method, Journal of computational Physics 32 (1) (1979) 101–136.

[41] S. McKee, M. F. Tomé, V. G. Ferreira, J. A. Cuminato, A. Castelo, F. Sousa, N. Mangiavacchi, The mac method, Computers & Fluids 37 (8) (2008) 907–930.

[42] G. Tryggvason, B. Bunner, A. Esmaeeli, D. Juric, N. Al-Rawahi, W. Tauber, J. Han, S. Nas, Y.-J. Jan, A front-tracking method for the computations of multiphase flow, Journal of computational physics 169 (2) (2001) 708–759.

[43] D. Lörstad, M. Francois, W. Shyy, L. Fuchs, Assessment of volume of fluid and immersed boundary methods for droplet computations, International journal for numerical methods in fluids 46 (2) (2004) 109–125.

[44] S. Osher, R. P. Fedkiw, Level set methods: an overview and some recent results, Journal of Computational physics 169 (2) (2001) 463–502.

[45] S. Osher, R. Fedkiw, Level set methods and dynamic implicit surfaces, Vol. 153, Springer Science & Business Media, 2006.

[46] J. A. Sethian, P. Smereka, Level set methods for fluid interfaces, Annual review of fluid mechanics 35 (1) (2003) 341–372.

[47] S. Majidi, A. Afshari, Towards numerical simulations of supersonic liquid jets using ghost fluid method, International Journal of Heat and Fluid Flow 53 (2015) 98–112.

[48] H. Forrer, R. Jeltsch, A higher-order boundary treatment for cartesian-grid methods, Journal of Computational Physics 140 (2) (1998) 259–277.

[49] R. B. Pember, J. B. Bell, P. Colella, W. Y. Curtchfield, M. L. Welcome, An adaptive cartesian grid method for unsteady compressible flow in irregular regions, Journal of Computational Physics 120 (2) (1995) 278–304.

[50] M. J. Berger, R. J. LeVeque, Stable boundary conditions for cartesian grid calculations, Computing systems in Engineering 1 (2-4) (1990) 305–311.

[51] P. Woodward, P. Colella, The numerical simulation of two-dimensional fluid flow with strong shocks, Journal of computational physics 54 (1) (1984) 115–173.

[52] G. Ben-Dor, I. Glass, Domains and boundaries of non-stationary oblique shock-wave reflexions. 1. diatomic gas, Journal of Fluid Mechanics 92 (3) (1979) 459–496.

[53] S.-M. Chang, K.-S. Chang, On the shock–vortex interaction in schardin's problem, Shock Waves 10 (5) (2000) 333–343.

[54] R. Boukharfane, F. H. E. Ribeiro, Z. Bouali, A. Mura, A combined ghost-point-forcing/direct-forcing immersed boundary method (ibm) for compressible flow simulations, Computers & Fluids 162 (2018) 91–112.

[55] H. F. Lehr, Experiments on shock-induced combustion, Astronautica Acta 17 (1972) 589–597.

[56] A. Harten, P. D. Lax, B. v. Leer, On upstream differencing and godunov-type schemes for hyperbolic conservation laws, SIAM review 25 (1) (1983) 35–61.

[57] C. K. Westbrook, Hydrogen oxidation kinetics in gaseous detonations, Combustion Science and Technology 29 (1-2) (1982) 67–81.

[58] J. McVey, T. Toong, Mechanism of instabilities of exothermic hypersonic blunt-body flows, Combustion Science and Technology 3 (2) (1971) 63–76.